INL/JOU-20-58661-Revision-0

Out-of-pile and postirradiated examination of lanthanide and lanthanide-palladium interactions for metallic fuel

February 2021

Michael T Benson, Jason Harp, Kevin R Tolman, Yi Xie, Tiankai Yao, Karen E Wright, James A King, Ayman Hawari, Qingsheng Cai

Changing the World's Energy Future

INL is a U.S. Department of Energy National Laboratory operated by Battelle Energy Alliance, LLC

INL/JOU-20-58661-Revision-0

Out-of-pile and postirradiated examination of lanthanide and lanthanide-palladium interactions for metallic fuel

Michael T Benson, Jason Harp, Kevin R Tolman, Yi Xie, Tiankai Yao, Karen E Wright, James A King, Ayman Hawari, Qingsheng Cai

February 2021

Idaho National Laboratory
Idaho Falls, Idaho 83415

http://www.inl.gov

Prepared for the
U.S. Department of Energy
Under DOE Idaho Operations Office
Contract DE-AC07-05ID14517

Out-of-pile and postirradiated examination of lanthanide and lanthanide-palladium interactions for metallic fuel

Michael T. Benson[a], Jason M. Harp[b], Yi Xie[c], Tiankai Yao[a], Kevin R. Tolman[a], Karen E. Wright[a], James A. King[a], Ayman I. Hawari[d], Qingsheng Cai[d]

[a]Idaho National Laboratory, P.O. Box 1625, MS 6188, Idaho Falls, ID 83415
[b]Oak Ridge National Laboratory, Oak Ridge, TN 37831
[c]Purdue University, 516 Northwestern Ave., West Lafayette, IN, 47906
[d]North Carolina State University, P.O. Box 7909, Raleigh, NC 27695

Corresponding Author Information

Michael T. Benson, phone: (208) 533-8870, email: michael.benson@inl.gov

Abstract

Palladium is being investigated as a fuel additive to bind with and potentially immobilize lanthanide fission products. A primary cause of fuel-cladding chemical interaction (FCCI) is the lanthanide fission products migrating to the fuel periphery and interacting with the cladding. This interaction will lead to wastage of the cladding and eventually to a cladding breach. Palladium has previously been identified as a promising additive used to prevent or decrease FCCI by reacting with the lanthanide fission products. In the current study, an alloy cast from the four highest abundant lanthanides found in irradiated metallic fuel, Nd, Ce, Pr, and La, with and without Pd, has been characterized using neutron diffraction, scanning electron microscopy, and electron probe microanalysis. In the lanthanide-Pd intermetallic compounds, all of the constituent compounds, i.e. Nd-Pd, Ce-Pd, La-Pd and Pr-Pd are known. There is very good agreement, both structurally and compositionally, between the out-of-pile lanthanide alloy and lanthanide fission products characterized in irradiated fuels. In both cases, the lanthanide elements form a solid solution in a hexagonal crystal structure. The out-of-pile lanthanide alloy follows Vegard's Law, with the measured and calculated (weighted average of constituents) lattice parameters being within 1% for both the a and c parameters. Pd bonds with the lanthanides (Ln) forming the phases LnPd and Ln_7Pd_3. The results indicate the properties of lanthanide compounds in irradiated metallic fuel can be reliably simulated in out-of-pile experiments.

Keywords: metallic nuclear fuel, fuel-cladding chemical interaction, neutron diffraction, lanthanide compound

1. Introduction

Fuel-cladding chemical interaction (FCCI) occurs when the nuclear fuel or fission products react with the cladding material. This interaction limits fuel performance by restricting the maximum temperature at which fuel can be operated. As more lanthanide fission products are created at higher burnups this performance limitation becomes more severe. Due to this, there are numerous investigations, both in-pile and out-of-pile, in the literature, as well as three recent review articles. Keiser recently published a historical perspective on FCCI, discussing the efforts over the last 70 years to understand and prevent FCCI to allow higher burnup and higher reactor operating temperatures [1], Matthews *et al.* published a review of FCCI in U-Pu-Zr metallic fuel [2], and Xie et al. published a review of the lanthanide migration mechanism in U-Zr metallic fuels [3]. A major cause of FCCI in U-Zr or U-Pu-Zr fuels during irradiation is fission product lanthanides (Ln), which move down the temperature gradient to the fuel periphery [2]. The result of this interaction is embrittlement and degradation of the cladding, which will eventually lead to rupture of the fuel rod.

Lanthanides can be present in a fuel during irradiation as fission products, but can also be present if the fuel was fabricated with recycled U. A small amount of lanthanides are expected in metallic fuel fabricated with recycled uranium [4]. Controlling FCCI in this system is even more important due to the early presence of lanthanides in the fuel. As soon as the fuel contacts the cladding due to swelling, at roughly 1-2% burnup [5], there are lanthanides available to react with the cladding and cause FCCI. This is opposed to the much slower generation of lanthanides solely from the fission process in a fuel fabricated without pre-existing lanthanides.

Several methods are being investigated to decrease or prevent FCCI, such as barrier foils [6], coatings [7][8], and additive materials [9-12]. After considering ways to bind lanthanides as stable intermetallics, a set of criteria were developed that identified Pd as a promising additive, especially since it is already a fission product [13]. The amount of fission product Pd is insufficient to bind the lanthanides, though, requiring additional Pd to be added to the alloy. In the chemical analysis of a U-10Zr fuel pin irradiated in EBR-II [13], the amount of Pd measured (0.05g) is very small compared to the quantity of lanthanides (1.73g, in an 81.47g sample). Recent work using Pd as an additive has shown promising results, both in-pile [14] and out-of-pile [13][15-17]. Lanthanide-Pd compounds have also been observed in irradiated U-10Zr when there is no added Pd, but only present as a fission product [18], lending credibility to this mitigation strategy. These compounds have also been observed in other metallic fuel alloys after irradiation [19-24]. The efficacy of fuel additives, specifically Pd, has been discussed in previous investigations [3][15][13].

The importance of FCCI in limiting the lifespan of nuclear fuel due to fission product lanthanides is known [2], although there has been no characterization of the lanthanides involved. No prior work in the literature has been performed to characterize the chemical structure of mixed lanthanide phases or mixed

lanthanide-palladium phases. This work is the characterization of two alloys, with one being a mix of 4 lanthanides, Nd, Ce, La, and Pr, and the other alloy being those lanthanides mixed with Pd. These alloys were characterized using neutron diffraction, scanning electron microscopy (SEM), and electron probe micro-analyzer (EPMA). These out-of-pile characterizations are compared against the characterization of lanthanides and lanthanide-Pd compounds in two irradiated fuels. The first fuel is an annular, helium bonded U-10Zr fuel pin irradiated in the Advanced Test Reactor to 3.3 % burnup [14], and the second is a solid, sodium bonded U-10Zr fuel pin irradiated to 5.7 % burnup (localized burnup) in the Fast Flux Test facility [16]. The composition and ratio of lanthanides used in the out-of-pile characterizations are based on elemental analysis of an irradiated U-10Zr EBR-II fuel pin [13], with the four most prevalent lanthanides included in the mix. In the chemical analysis, only elements above 0.01g were included, which encompassed 6 lanthanides (La, Ce, Pr, Nd, Pm, Sm). The four highest abundance (Nd, Ce, La, and Pr) lanthanides are 92% of the measured lanthanide fission products. The ratio obtained from the EBR-II fuel is approximately 53Nd-25Ce-16Pr-6La, in wt. %.

2. Experimental Methods

Post-irradiation examinations (PIE) were performed on two U-10Zr fuel samples, focusing on phase analysis and the chemical composition of Ln precipitates. A rough estimate, based on Origen2 calculations [25], of the expected quantity of Pd, Nd, Ce, Pr, and La produced as fission products in each irradiated fuel is listed in Table 1, along with basic details of the fuel. The total lanthanides produced are 1.2E-03 mol/mol fuel in the annular U-10Zr fuel pin, and 3.2E-02 mol/mol fuel in the MFF-3 U-10Zr fuel pin.

Table 1. Irradiated fuel details, with atomic concentration of selected fission products in the fuel (in mol/mol fuel).

	Burnup	Bonding agent	Pd	Nd	Ce	Pr	La	Cs	Ba
Annular U-10Zr	3.3 at. %	Helium	7.3 E-05	4.9 E-04	3.8 E-04	1.6 E-04	1.7 E-04	5.1E-04	1.9E-04
MFF-3 U-10Zr	5.7 at. %	Sodium	2.8 E-03	1.4 E-02	8.4 E-03	4.2 E-03	4.5 E-03	1.2E-02	6.6E-03

The first irradiated sample is an annular U-10Zr fuel that was irradiated to 3.3 at. % burnup in the Advanced Test Reactor (ATR). Initial characterization of this fuel pin (not including advanced techniques such as electron microscopy) has been previously reported [14]. As described in the previous report, this fuel pin was removed from the reactor early due to variations in the inner diameter of the cladding causing the fuel to run hotter than expected. Helium has very poor thermal conductivity, so a helium-bonded fuel cannot tolerate large fuel-cladding gaps. The issues in the rodlet assembly were corrected in

subsequent annular fuel rods, and this fuel pin, even though it ran hot, has provided an initial look at this novel fuel design. A transmission electron microscope (TEM) sample that covers both the U matrix and Ln precipitate was prepared using focused ion beam (FIB) in a FEI Quanta 3D FEG Dual Beam (SEM/FIB). A 2 KeV Ga ion beam was used for final polishing prior to transferring the sample into the TEM. Electron diffraction (ED) patterns and STEM EDS data were collected at room temperature using a Thermo Fisher™ Talos F200X scanning/TEM (STEM) operated at 200 KeV. EDS data was collected in the scanning mode using four Super-X windowless EDS detectors based on ChemiSTEM technology, with the beam size < 1 nm. SEM images of the irradiated annular U-10Zr fuel were also obtained on the FEI Quanta 3D FEG Dual Beam (SEM/FIB).

The second post-irradiation sample is U-10Zr, from the MFF-3 assembly irradiated in the Fast Flux Test Facility (FFTF) [26]. The post-irradiation examination (PIE) of this specific fuel pin has been previously reported [18][27]. This assembly had a peak inner cladding temperature of 643 ºC and operated to 13.8 at. % burnup. The slice used for SEM analysis was taken at x/L=0.98 (fuel pin length=91.4cm) from fuel pin serial number 193045. The local burnup for the sample was 5.7 at. % and the time averaged temperature of the inner cladding for the sample was 615 °C [27].

Two alloys were cast, one with four lanthanides, Nd, Ce, Pr, and La, and another alloy containing those lanthanides and Pd. The alloy compositions are listed in Table 2. Materials were obtained from Alfa Aesar and used as received. The lanthanides were obtained as rods, packaged in mylar under argon. Even packaged under argon, some oxidation was visible on the surface of the Ce and La rods. There were no attempts to clean the rods, and they were used as received. The specific lanthanide composition is roughly based on the chemical analysis of an EBR-II U-10Zr irradiated fuel pin (8% burnup) [13], using the ratio of the four most prevalent lanthanides. The Pd content is based on the SEM analysis of a Pd-Ln precipitate in a U-10Zr fuel pin irradiated in FFTF, as described more fully below. For simplicity, the alloys will be referred to as the Ln alloy, or the Ln-Pd alloy.

Table 2. Alloy compositions

Alloy	Composition (wt. %)	Composition (at. %)
Ln	53Nd-25Ce-16Pr-6La	52.3Nd-25.4Ce-16.2Pr-6.1La
Ln-Pd	39.8Nd-18.8Ce-12Pr-4.0La-25.0Pd	36.2Nd-17.6Ce-11.2Pr-4.3La-30.7Pd

All casting operations were carried out in an arc-melter within an argon atmosphere glovebox with high purity argon as a cover gas. To cast the Ln alloy, the appropriate amount of Nd, Ce, Pr, and La were arc melted together in one step. To cast the Ln-Pd alloy, the appropriate amount of a Ln pre-alloy was mixed with Pd. In each case, after melting the constituents together, the resulting button was flipped and re-melted three times to ensure homogeneity, which was verified visually when performing the SEM analysis. The buttons were cast into 5 mm diameter pins.

Approximately 1.5” were taken from each pin and loaded into separate 0.250” x 2.00” vanadium sample cans (Metal Technologies) for neutron diffraction studies. All processing of the lanthanides, from opening the mylar packages to loading the samples cans, was performed in an argon glovebox. Scanning electron microscopy (SEM) was performed on a section of the Ln-Pd pin mounted in a 31.8 mm diameter phenolic metallographic (met) mount filled with epoxy. Samples were polished by grinding the surfaces flat with SiC grinding paper followed by polishing with polycrystalline diamond suspensions, starting with 9 μm, then 3 μm, and finally 1 μm. The polished sample was analyzed with a sputtered coating of approximately 15 nm carbon to control charging of the met mount.

Two instruments were utilized for SEM analysis. The SEM instrument used for non-irradiated analysis was a JSM-7600f SEM, while the MFF-3 sample irradiated at FFTF was analyzed using a JSM-7000f SEM. Both instruments were manufactured by the Japan Electron Optics Laboratory (JEOL), and are hot field emission SEMs equipped with Oxford Instruments X-Max 20 silicon drift energy dispersive X-ray spectrometers (EDS) and Nordlys II F+ electron back scattered diffraction cameras. Both SEMs were operated at an accelerating voltage of 20 keV. The X-ray spectrometers are controlled by Oxford INCA software (v. 4.15, part of the Oxford Microanalysis Suite Issue 18d + SP 4), which also provides image acquisition capabilities. Spectra were collected over the energy range 0 – 20 keV, which covers characteristic X-ray energies from all analytes. Spectra were quantified using so-called “standardless” analysis, which uses a stored library of reference spectra to quantify unknown spectra rather than physical standards. This method is generally accurate to the 0.1 to 0.5 w/w% range, depending on sample and microscope (observation) conditions. Quantitative results for the Ln-Pd alloy were normalized to Pd, Nd, Ce, Pr, and La.

Compositional analyses were acquired on a CAMECA SX100R electron probe microanalyzer (EPMA) equipped with four tunable wavelength dispersive spectrometers. A focused beam with an accelerating voltage of 20 kV and current of 101 nA was used on each point. Analytical conditions are listed in Table 3. Quantitative point analysis was performed using Probe for EPMA v. 11.8.8. The mass absorption coefficients dataset was FFAST [28], and the phi-rho-Z algorithm utilized was Pouchou and Pichoir-Full [29]. Results are from single points and detection limits ranged from 0.035 wt. % for O kα to 0.043 wt. % for La lα to 0.070 wt. % for Ce lα. The single point detection limit calculation (Equation 1) is based on the standard counts and the unknown sample background counts and include the magnitude of the ZAF correction factor. The calculation is adapted from Ref. [30], and is useful in that it can be used even on inhomogeneous samples and can be quoted as the detection limit in weight percent for a single analysis line with a confidence of 99% (assumes 3 standard deviations above the background).

$$CDL = (ZAF)\ (3/I_s)\ (SQRT\ (I_b * 100)) \qquad \text{(Eq. 1)}$$

CDL is the calculated detection limit with a 99% (3-sigma) confidence, ZAF is the ZAF correction factor for the sample matrix, I_s is the count rate (cps/nA) on the pure element standard (apply std k-factor), and I_b is the background count rate (cps/nA) on the unknown sample. In Equation 1, before calculating the SQRT of the background count rate, the count rate (cps/nA) must first be denormalized to raw counts with the beam current and integration time for the unknown intensity. After calculating the SQRT, the background must be re-normalized to cps/nA before calculating the above k-ratio I_B/I_S.

After obtaining quantitative X-ray maps on the EPMA, an analysis of each of the 47,000 map pixels was performed using a Hartigan-Wong k-means clustering algorithm, providing a modal analysis of phases and quantities present. In this algorithm, the user specifies the components to use for classification, the number of clusters and the desired precision. The program then calculates a statistical representation of the area percentage of each cluster, which corresponds to a phase. After inputting the density of each phase, the program calculates the mass percent of each phase in the X-ray map.

Table 3. Analytical parameters employed for EPMA quantitative pint analysis.

X-ray	Crystal	Peak Time (s)	Background time (s)	Corrected overlap	Standard
O Kα	PC1	30	20		NdP_5O_{14}
Pd Lα	PET	20	20		Pd
Nd Lα	LiF	20	20		NdP_5O_{14}
Ce Lα	LiF	30	20		CeP_5O_{14}
Pr Lα	LiF	30	20	La	PrP_5O_{14}
La Lα	LiF	60	60	Nd	LaP_5O_{14}

Neutron diffraction measurements were carried out at the PULSTAR Neutron Powder Diffractometer at North Carolina State University. The PULSTAR reactor is a swimming pool reactor with maximum power 1 MW. The diffractometer is located at beam tube 4 of the reactor. A double focusing monochrometer, which can focus two-dimensional neutrons to the sample position, is employed in this facility. The flux of neutrons with wavelength 1.489 Å is $0.5x10^5$ n/ cm^2s at the sample position. A 15 position sensitive detector array attached to a moveable cassette can span 20° (a section) and can be moved from 15° to 115° to cover the entire scattering angle of 5°-125°. A fission chamber located at the beam before the sample is employed as the monitor. The detectors collect data at each section for a fixed monitor count to ensure the incoming neutrons at the sample position is the same for each section. The data from the 6 sections are collated into the full scattering angle range data. The neutron powder diffraction data was analyzed using Rietveld method [31] with the GSAS program [32].

3. Results

3.1 PIE of irradiated annular U-10Zr

Basic PIE has been reported for the annular U-10Zr fuel pin, including neutron radiography, evaluation of the distribution of gamma-ray emitting radionuclides, dimensional inspection, fission gas release analysis, optical microscopy, and chemical analysis [14]. Advanced PIE (SEM and TEM) of the fuel pin [33] and the fuel-cladding interface [34] have also been reported. This manuscript focuses on characterization of lanthanide, and lanthanide-Pd compounds, thus only the characterized lanthanide precipitates are within the scope of this investigation.

A montage image of the annular U-10Zr fuel pin section is shown in Figure 1a, along with the location where the lamella was lifted, indicated by the red rectangle. The location is just outside of the central, Zr-rich region. Originally this was the annulus of the fuel, but filled in during irradiation as the fuel swelled and fission gas bubbles developed. NOTE: The sample was polished prior to loading into the FIB to remove the oxide layer. Due to this, the montage image shown in Figure 1a does not exactly match the image shown in Figure 1b. The location of the lamella is accurate based on remaining larger features on the surface.

Figure 1b and Figure 1c show magnified images of where the lamella was lifted. The lanthanides were observed as nodules around the periphery of pores, as indicated in Figure 1c with red arrows. The lamella was lifted from the edge of a pore, which included a lanthanide nodule and U matrix. The thinned lamella is shown in Figure 1e, with the lanthanide nodule on the right side of the lamella, while the left side is U matrix. The lower right side of the lamella split away during thinning, and it is this small section of the lanthanide nodule that has been further investigated. EDS mapping of this section is shown in Figure 2 for Ba, Nd, Ce, Zr, and La, with the region indicated by the white rectangle. Ba is found on the left side of this region, between the lanthanide nodule and the U matrix. The lanthanides are evenly distributed throughout the nodule, with the only variations occurring where there is a higher concentration of Ba. The yellow rectangle indicates the location of quantitative STEM EDS analysis, with the results listed in Table 4.

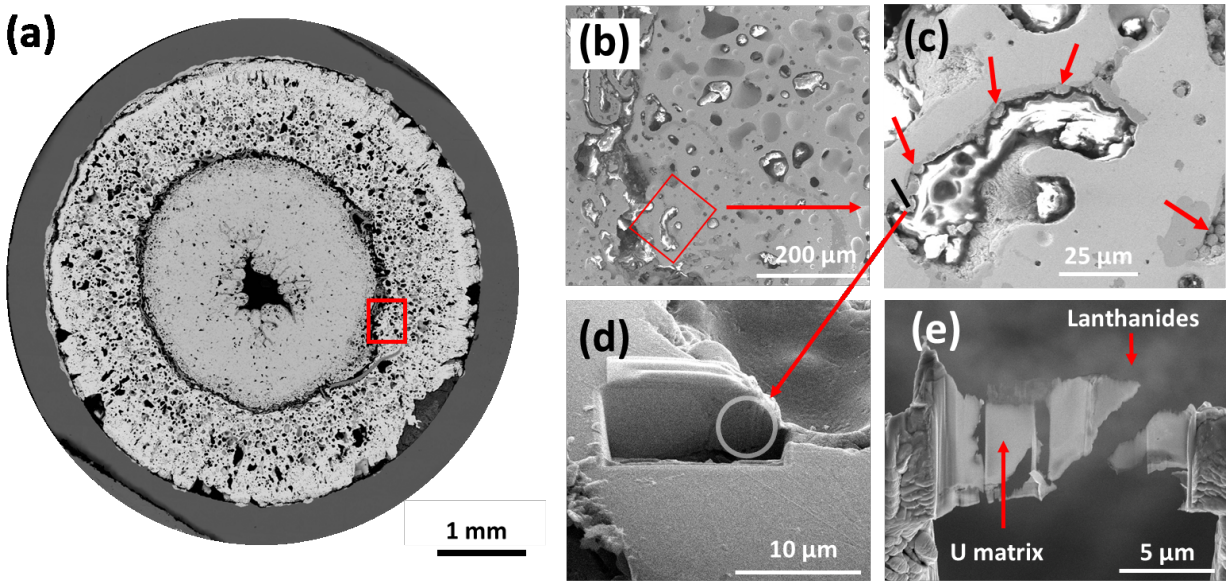

Figure 1. a. Montage image of irradiated annular U-10Zr. Red rectangle indicates location of image shown in 1b. Red rectangle in 1b indicates location of image shown in 1c. The black line indicates the location of the lamella. The red arrows in 1c indicate nodular lanthanide precipitates. 1e shows an image of the final lamella after thinning.

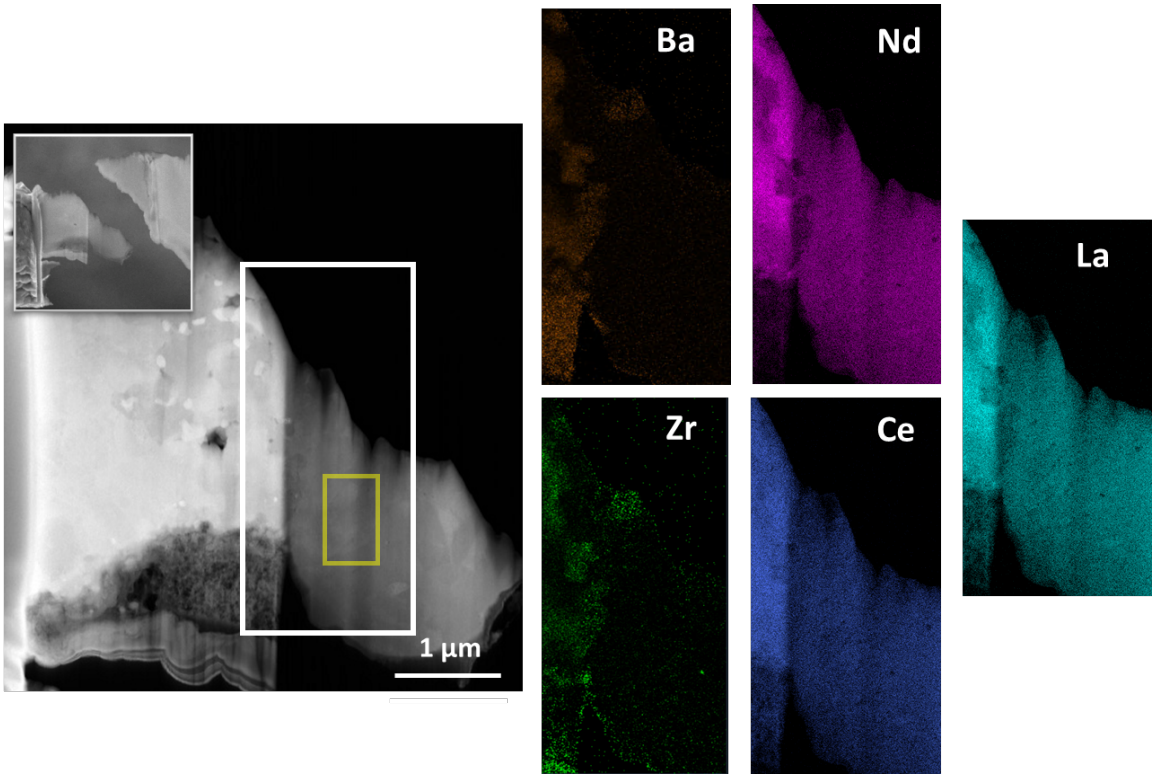

Figure 2. TEM EDS mapping of lanthanide precipitate. The white rectangle indicates the mapping region, and the yellow rectangle indicates the location of quantitative EDS analysis, with the results listed in Table 4.

Table 4. STEM EDS analysis for region indicated by yellow rectangle in Figure 2.

element	at. %
Y	2.1
Zr	7.7
La	14.2
Ce	21.5
Pr	4.1
Nd	48.8
Sm	1.5
U	0.1

To identify phase, diffraction patterns were taken from the Ln grains. A brightfield TEM image showing the location of two collected diffraction patterns is shown in Figure 3, with the diffraction patterns included as inserts. Indexing of these patterns indicates the Ln precipitates are in a hexagonal crystal structure, with lattice parameters calculated to be a = 3.89 Å and c = 12.55 Å, based on the interplanar distance in the diffraction patterns. The diffraction patterns shown are very clean, with no indication of oxidation during sample transfer between the FIB and TEM. Oxidation is always a concern due to the extremely oxophilic nature of the lanthanides.

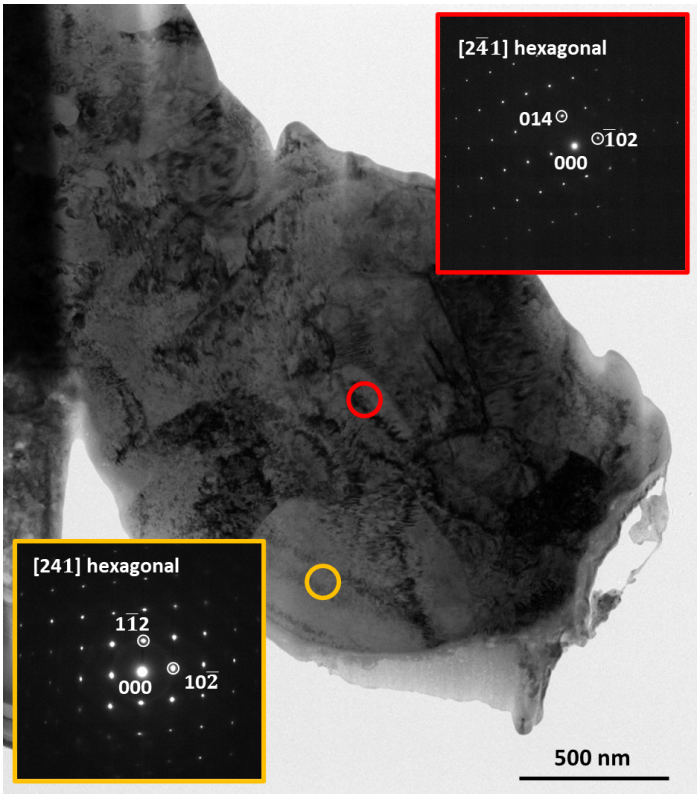

Figure 3. TEM brightfield image showing locations (circles) of diffraction analysis in the lanthanide precipitate, with the diffraction patterns included.

3.2 PIE of irradiated solid U-10Zr

The full characterization of U-10Zr MFF3 pin #193045 has been previously reported [18][27], and is only included here as an example of Pd-lanthanide precipitates in an irradiated fuel. The post-irradiation microstructure for this fuel pin is shown in Figure 4. This SEM image was obtained from the central, Zr-rich region of the fuel pin. The majority of the microstructure is a mixture of α-U and δ-UZr_2, with this region of the fuel being approximately 30 to 35 wt. % Zr by EDS analysis. The enhanced concentration of Zr in this area is due to the well-known phenomenon of Zr redistribution in irradiated U-Zr fuels [18]. A key feature of the microstructure shown in Figure 4 is the dark grey precipitates highlighted by the red circles. The composition of the precipitates, as determined by EDS analysis, is listed in Table 5. The presence of these lanthanide-Pd precipitates in this sample with fission product generated Pd is encouraging for the feasibility of this FCCI mitigation strategy. Due to the low fission yield of Pd compared to the lanthanides, not all of the observed lanthanide deposits in this fuel contained Pd.

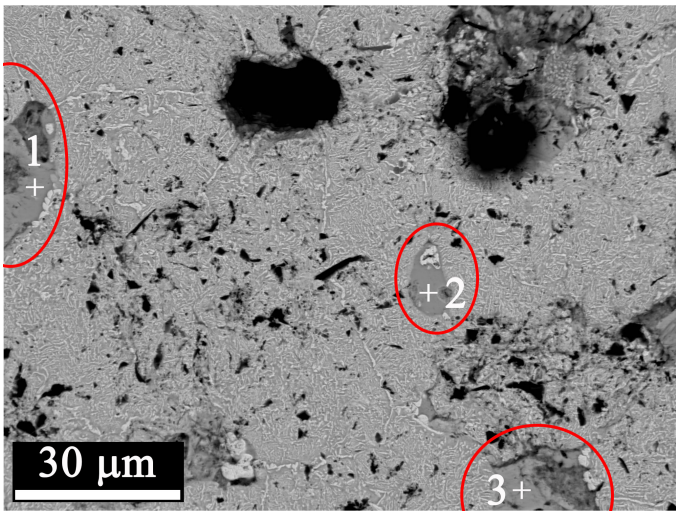

Figure 4. SEM backscatter image of FFTF U-10Zr fuel, post-irradiation [18]. The red circles indicate Pd-Ln precipitates. Corresponding EDS data are listed in Table 5.

Table 5. EDS data for points shown in Figure 4. Values in at. %.

	U	Pd	Nd	Ce	La	Y	Sm
1	0	31	35	13	9	8	4
2	1	32	36	14	8	9	0
3	0	31	38	15	10	6	0

3.3 SEM characterization of non-irradiated samples

A representative SEM backscatter image of the Ln-Pd alloy is shown in Figure 5a, with a magnified image shown in Figure 5b. The EDS points shown, with data listed in Table 6, are for the

matrix region and the precipitates. The microstructure shows large Pd-rich inclusions, and black intergranular regions. The intergranular boundaries contain lanthanide oxides. Although the lanthanide rods were packaged under argon in mylar bags, Ce and La still had some oxide on the surface, significantly more than Nd and Pr. No attempts to clean the raw materials were made and are the likely source of the oxide. The oxides are mixed throughout the pins, indicating the oxide was present prior to or during arc melting. The composition of the oxides varied, although in general the intergranular oxides, indicated with red arrows in Figure 5b, are comprised of Ce, Pr, and La. The larger black spots, indicated with blue arrows, are Nd_2O_3.

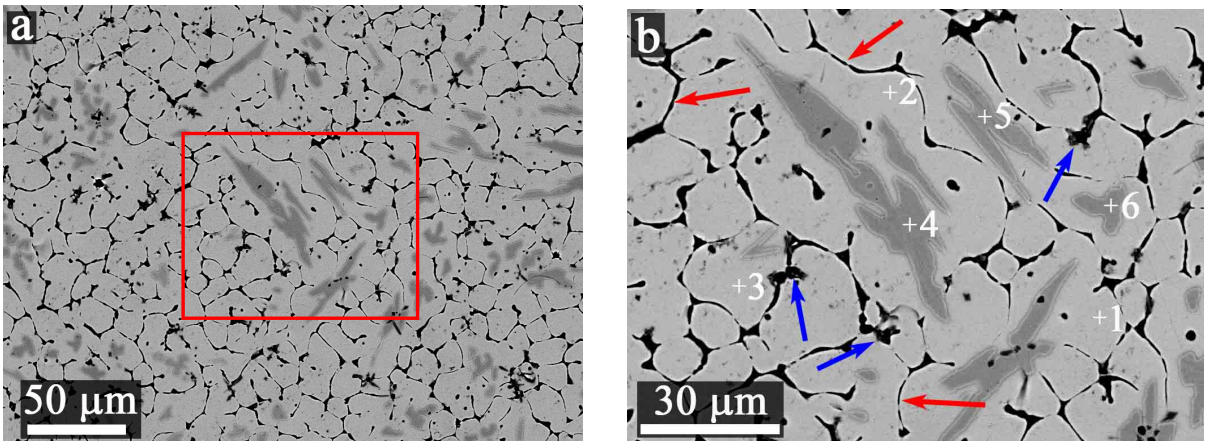

Figure 5. a. and b. SEM backscatter images for the Ln-Pd alloy. The red rectangle in 5a indicates the magnified region shown in 5b. Corresponding EDS results are listed in Table 6. Red arrows indicate representative regions of Ce, La, and Pr oxides. Blue arrows indicate representative areas of Nd_2O_3.

Table 6. EDS analysis results for points shown in Figure 5b. Values shown in at. %.

	Nd	Ce	Pr	La	Pd	Phase[a]
1	35	18	10	5	32	Ln_7Pd_3
2	35	18	11	4	32	Ln_7Pd_3
3	35	18	10	5	32	Ln_7Pd_3
4	30	9	7	2	52	LnPd
5	30	9	7	2	52	LnPd
6	30	9	7	2	52	LnPd

[a] Suggested phase based on EDS analysis

3.4 EPMA characterization of non-irradiated samples

In the SEM EDS analysis, differences in Lα peak energy between each of the lanthanides (La to Ce, Ce to Pr, and Pr to Nd) is consistent at roughly 0.19 keV, causing a significant amount of peak overlap. There is also significant peak overlap for the lanthanides in the neutron diffraction data discussed below. In order to accurately determine the elemental composition of the phases, quantitative EPMA was performed using standards for each element.

EPMA analysis was performed on the two primary phases in the Ln-Pd alloy, shown in Figure 5b, i.e. the light grey areas (Ln_7Pd_3), and the dark grey areas (LnPd), and on the intergranular oxide. For the two primary phases, ten spots were quantitatively analyzed, while for the oxide, three spots were analyzed, with the results listed in Table 7. The oxide analysis listed in Table 7 does not include oxygen, due to interference from surface oxidation. For each of the phases, the ratio of lanthanides present in the phase is used in the discussion. For this reason, excluding oxygen, which will be erroneous due to surface oxidation, does not affect the resulting discussion. Using a cluster analysis, as described in the experimental section, the amount of each phase on the surface was determined to be 79.0 % of the Ln_7Pd_3 phase, 12.0 % of the LnPd phase, and 9.0 % of the oxide phase.

Table 7. EPMA measured elemental compositions in the Ln-Pd alloy. All values in at. %.

Point	Nd	Ce	Pr	La	Pd
Ln_7Pd_3					
1	36.9	17.2	11.4	4.4	30.1
2	36.8	17.3	11.5	4.4	30.0
3	37.1	17.2	11.4	4.4	29.9
4	37.1	17.3	11.3	4.4	29.9
5	37.2	17.2	11.4	4.5	29.8
6	36.8	17.6	11.3	4.5	29.8
7	37.3	17.3	11.4	4.4	29.6
8	37.3	17.2	11.4	4.4	29.8
9	37.0	17.2	11.5	4.4	29.9
10	37.1	17.3	11.4	4.3	30.0
Average	37.1	17.3	11.4	4.4	29.9
LnPd					
1	31.4	9.0	7.8	2.2	49.6
2	31.3	9.2	7.7	2.2	49.7
3	31.2	9.1	7.7	2.2	49.7
4	31.2	9.0	7.7	2.3	49.8
5	31.3	8.9	7.7	2.2	49.9
6	31.4	9.0	7.7	2.2	49.7
7	31.5	8.8	7.7	2.1	49.8
8	31.9	9.5	7.8	2.3	48.6
9	31.5	8.8	7.8	2.1	49.8
10	31.6	9.2	7.7	2.2	49.3
Average	31.4	9.1	7.7	2.2	49.6
Oxide[a]					
1	37.3	36.4	16.3	7.9	2.1
2	38.3	35.6	16.3	7.8	2.0
3	37.6	35.4	16.3	7.8	2.9
Average	37.7	35.8	16.3	7.9	2.3

[a] Oxide compositions are normalized without oxygen.

3.5 Neutron Diffraction characterization of non-irradiated samples

Attempts were made to characterize the alloys with X-ray diffraction. The extremely oxophilic nature of the lanthanides prevented data collection prior to oxidation, even with coatings to prevent oxidation. Due to this, neutron diffraction, with the samples sealed in vanadium sample cans under argon, was used to characterize the alloys.

Figure 6 and Table 8 show the neutron diffraction results for the single phase Ln alloy refined in the hexagonal structure with space group $P6_3/mmc$, Joint Committee on Powder Diffraction Standards (JCPDS) 04-020-6110 [35]. The lattice parameters, fractional coordinates, occupancies, and thermal parameters (Uiso) are listed in Table 8. The assumption that the lanthanides were all in special positions was in good agreement with JCPDS 04-020-6110 and had a goodness-of-fit of wRp = 0.058 and Chi^2 = 3.30. The artifact peaks at 34.02°, 48.89° (marked with *) suggest a minor presence of the cubic oxide phase based CeO, *Fm-3m* (JCPDS 04-007-4020 and 04-003-5175). An additional peak at 60.90° is not evident due to surrounding peaks.

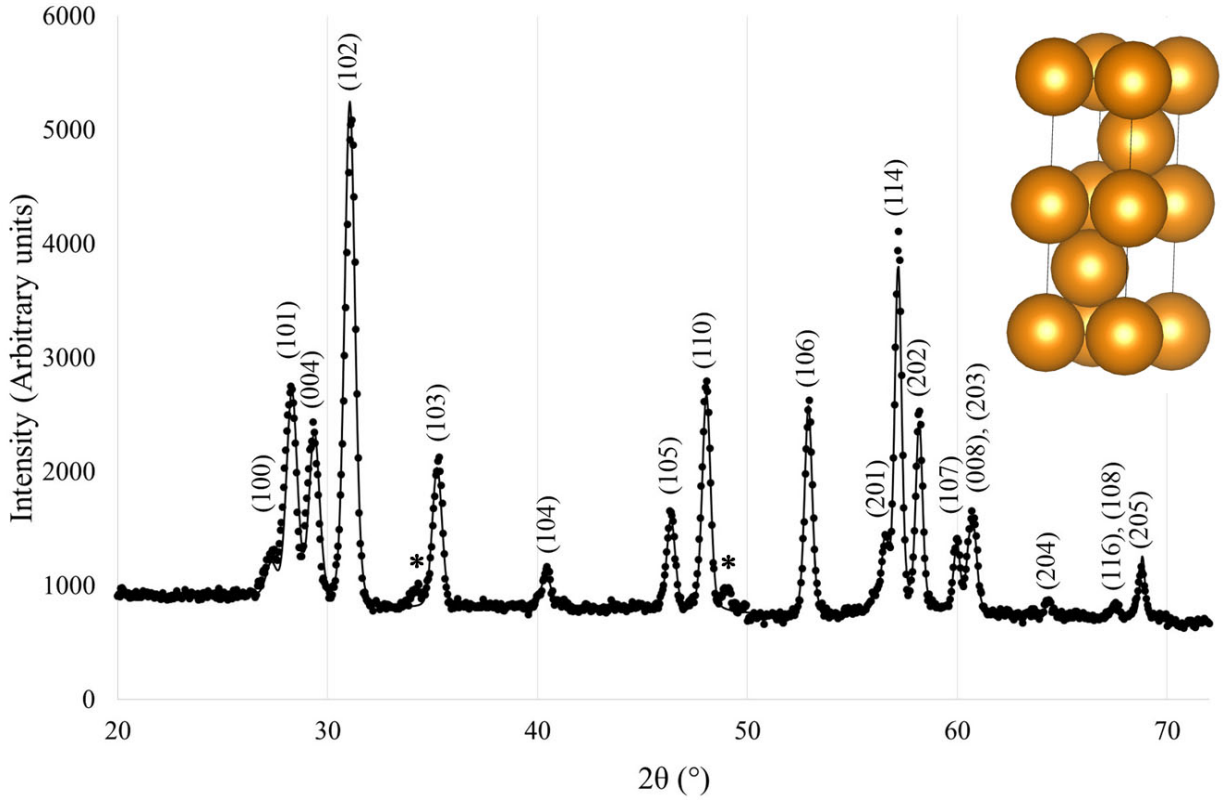

Figure 6. Neutron diffraction pattern for Ln alloy. The inset shows the unit cell structure for this compound. All peaks correspond to a hexagonal structure.

Table 8. Refinement results for Ln alloy in $P6_3/mmc$: RT 28M.

a (Å)	*b (Å)*	*c (Å)*	α	β	γ	Vol. (Å^3)

3.6774(4)	3.6774(4)	11.8563(5)	90°	90°	120°	138.86(12)
Label	Wyckoff	*x*	*y*	*z*	Occ.	Uiso
La	2a	0.00	0.00	0.00	0.0707(11)	0.0194(43)
Nd	2a	0.00	0.00	0.00	0.5311(15)	0.0163(80)
Pr	2a	0.00	0.00	0.00	0.1661(11)	0.0229(84)
Ce	2a	0.00	0.00	0.00	0.2537(12)	0.0236(46)
La	2c	0.3333	0.6667	0.25	0.0758(74)	0.0248(40)
Nd	2c	0.3333	0.6667	0.25	0.5357(15)	0.0098(79)
Pr	2c	0.3333	0.6667	0.25	0.1667(38)	0.0199(84)
Ce	2c	0.3333	0.6667	0.25	0.2543(30)	0.0141(46)

Figures 7 and 8 and Tables 9 and 10 show the neutron diffraction results for the Ln-Pd alloy, containing two phases. The primary phase had a Nd_7Pd_3 structure and was refined in the hexagonal structure with space group $P6_3mc$ (JCPDS 04-001-1116). The lattice parameters, fractional coordinates, occupancies, and thermal parameters (Uiso) for space group $P6_3mc$ are listed in Table 9. The secondary phase had a LaPd orthorhombic structure and was refined with space group *Cmcm* (JCPDS 04-004-3283). The lattice parameters, fractional coordinates, occupancies, and thermal parameters (Uiso) for space group *Cmcm* are listed in Table 10. The assumption that the lanthanides had the same atomic positions showed a goodness-of-fit of wRp = 0.053 and $Chi^2 = 3.40$. Peaks for lanthanide oxides, such as the artifact peaks observed in the Ln alloy, shown in Figure 6, for CeO, or peaks for Nd_2O_3 (28.99º, 38.19º, and 53.52º, trigonal *P*321 Nd_2O_3, JCPDS 04-015-5004) are likely present, but are not observed due to peak overlap. The same arc melted pin produced the neutron diffraction sample as well as the sample for SEM analysis, shown in Figure 5, so an intergranular oxide is present in the sample, but not in high enough concentration to observe through the Ln-Pd peaks.

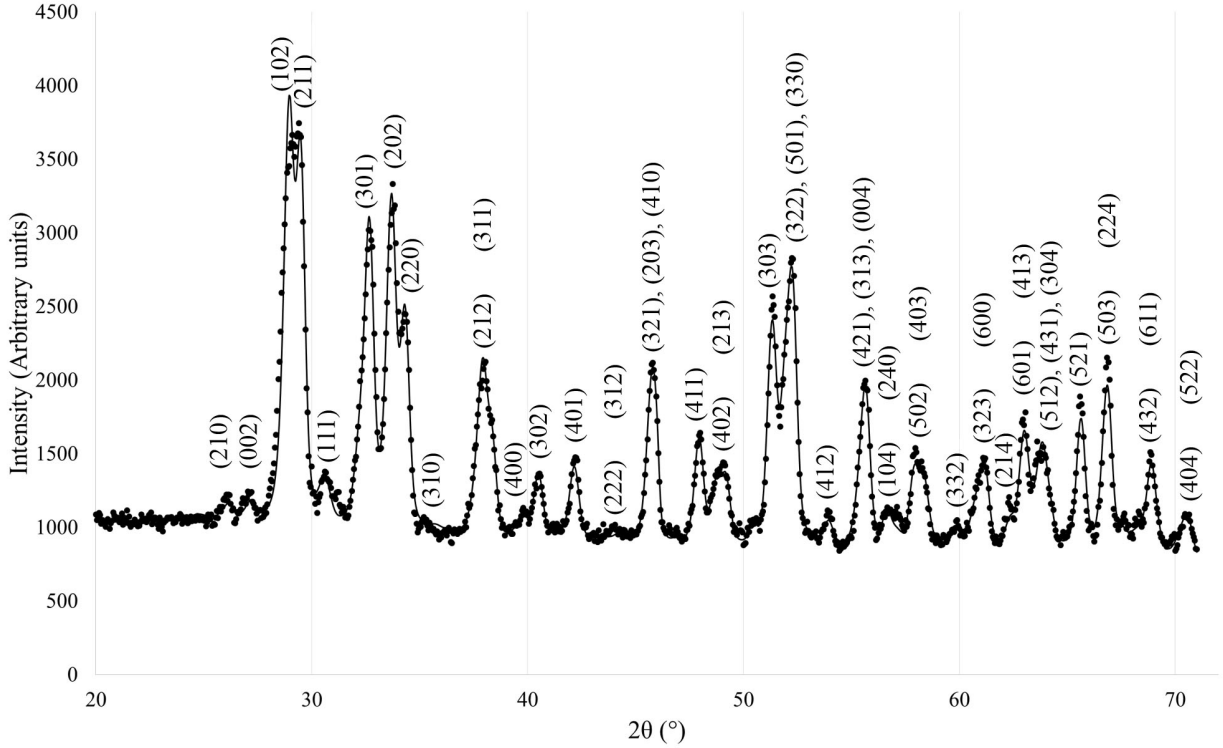

Figure 7. Neutron diffraction pattern for Ln-Pd alloy. All peaks correspond to a hexagonal structure except for (111) and (240), which are orthorhombic.

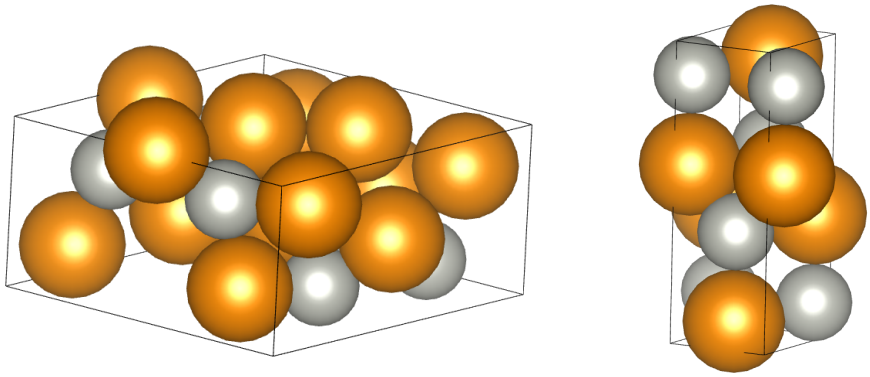

(a) (b)

Figure 8. Illustrations for primary and secondary unit cell structures for Ln-Pd alloy. (a) unit cell from hexagonal $P6_3mc$ Ln_7Pd_3 phase, and (b) unit cell from orthorhombic *Cmcm* LnPd phase. Silver spheres represent Pd, orange spheres represent Ln.

Table 9. Primary phase refinement results for Ln-Pd alloy in $P6_3/mmc$: RT 28M.

a (Å)	*b* (Å)	*c* (Å)	α	β	γ	Vol. (Å^3)
10.1683(7)	10.1683(7)	6.3996(4)	90°	90°	120°	573.04(8)

Label	Wyckoff	*x*	*y*	*z*	Occ.	Uiso
La	2b	0.3333	0.6667	0.0410(5)	0.0384(12)	0.0121(19)
Ce	2b	0.3333	0.6667	0.0410(6)	0.1276(84)	0.0120(21)
Pr	2b	0.3333	0.6667	0.0410(5)	0.0915(67)	0.0121(11)

Nd	2b	0.3333	0.6667	0.0410(6)	0.2636(54)	0.0099(19)
La	6c	0.1224(5)	0.8776(7)	0.25	0.0405(29)	0.0255(43)
Ce	6c	0.1224(3)	0.8776(4)	0.25	0.1267(16)	0.0255(42)
Pr	6c	0.1224(3)	0.8776(3)	0.25	0.0963(10)	0.0255(45)
Nd	6c	0.1224(4)	0.8776(5)	0.25	0.2456(53)	0.0238(48)
La	6c	0.5341(6)	0.4659(7)	0.0366(5)	0.0387(16)	0.0191(22)
Ce	6c	0.5341(5)	0.4659(3)	0.0366(7)	0.1310(47)	0.0190(16)
Pr	6c	0.5341(7)	0.4659(5)	0.0366(5)	0.0954(12)	0.0191(23)
Nd	6c	0.5341(6)	0.4659(2)	0.0366(4)	0.2641(54)	0.0182(18)
Pd	6c	0.8090(5)	0.1910(6)	0.2947(3)	0.4768(67)	0.0176(28)

Table 10. Secondary phase refinement results for Ln-Pd alloy in *Cmcm*: RT 28M.

a (Å)	*b (Å)*	*c (Å)*	α	β	γ	Vol. (Å^3)
3.8330(35)	10.8153(11)	4.6222(44)	90°	90°	90°	191.61(32)

Label	Wyckoff	*x*	*y*	*z*	Occ.	Uiso
La	4c	0.00	0.4211(3)	0.25	0.0360(23)	0.0014(13)
Ce	4c	0.00	0.4211(2)	0.25	0.1502(40)	0.0242(23)
Pr	4c	0.00	0.4211(2)	0.25	0.0508(19)	0.0265(18)
Nd	4c	0.00	0.4211(4)	0.25	0.2142(60)	0.0320(40)
Pd	4c	0.00	0.1287(2)	0.25	0.4042(43)	0.0242(26)

4. Discussion

In all three irradiated fuel pins, Nd is found to be the dominant lanthanide element followed by Ce, making up over 70% atomically of the fission product lanthanides as would be expected from known fission yields. Most importantly, the formation of low melting intermetallic compounds between Fe and Ce is a primary reason for cladding wastage, limiting the maximum operating temperature of high burnup U-Zr metallic fuels. The expected yields for Pd, Nd, Ce, Pr, and La for the FFTF irradiated and ATR irradiated U-10Zr fuel pins are listed in Table 1. Based on the EBR-II chemical analysis [13] and the expected elemental atomic concentrations for the annular and the solid fuel pins, the lanthanides are produced in much higher abundance than fission-product Pd. This was expected, since the lanthanides are produced by fission in a higher yield than Pd regardless of the fissioning actinide or the neutron energy spectrum in a nuclear reactor. Due to these atomic concentrations, the composition of the Ln-Pd precipitates observed in the MFF-3 irradiated U-10Zr fuel pin are lanthanide rich, with Pd being ~31 at. %, Table 6. This composition will primarily produce Ln_7Pd_3, with a small amount of LnPd, based on the Nd-Pd phase diagram [36]. Note: The Nd-Pd binary phase diagram is the most complete diagram of the constituent Ln-Pd diagrams, and will be used for phase discussions. In the annular U-10Zr fuel pin irradiated in ATR, no Pd was observed in the Ln precipitates. Table 1 indicates only slightly less Pd will be produced as in the MFF-3 irradiated pin. A thorough search of the annular fuel pin may reveal Ln-Pd precipitates, but in this investigation, none of the lanthanide nodules analyzed contained Pd.

The lanthanide deposits in the outer area of the annular U-10Zr fuel, i.e. the radial region containing the red box in Figure 1a, occur at the periphery of pores, and are present as nodules, as indicated with red arrows in Figure 1c. This may support the proposed liquid like transport of lanthanides through the interconnected porosity that forms during irradiation [3][13][37][38][39]. Typically, this would occur due to either sodium or a sodium-cesium mix present in the pores, but as this is a sodium-free fuel, the liquid-like transport mechanism can still proceed due to fission product cesium in the pores. During sample preparation methods, methods were not employed to preserve Cs, thus it was washed away during the cutting or polishing step. Barium, a decay product of Cs, is observed, though, and is co-located with the lanthanide nodules in the pores. This is shown in the elemental map for Ba in Figure 2. Having Cs present without Na may be beneficial for transport, though, since the lanthanides have a higher solubility in Cs at reactor temperature than in Na [37-39]. The solubility is roughly 5 at. % at 600 °C based on the Cs-Pr phase diagram [40], which is the only available lanthanide-Cs phase diagram for the constituents in the Ln mix. No comparable phase diagrams are available for the lanthanide-Na systems. The lanthanides are not soluble at room temperature, though, which accounts for the precipitation around the pore periphery.

The composition of the Ln-Pd precipitates observed in the MFF-3 irradiated U-10Zr fuel pin was the basis for the out-of-pile experiments described herein. In previous out-of-pile investigations with Pd as a minor additive to bind the lanthanides and control FCCI [13][15-17], enough Pd was added to bind the lanthanides in a 1:1 Ln-Pd compound. The rational for this amount of Pd is discussed in Ref. [13], while the later studies maintained this Pd:Ln ratio for consistency [15-17]. This does not indicate a 1:1 compound is required for Pd to bind the lanthanides, considering the Ln_7Pd_3 compound formed in the irradiated U-10Zr fuel pin. Just based on the amount of lanthanides captured per Pd atom, the Ln_7Pd_3 compound is the most efficient use of Pd, although this compound has the lowest solidus temperature (620°C) of any of the possible intermetallic compounds, based on the Nd-Pd phase diagram [36]. Depending on the radial location of this compound in a fuel during irradiation, this phase may be a liquid. Providing excess Pd also has drawbacks, although the solidus temperatures are much higher than Ln_7Pd_3. Prior to reacting with fission product lanthanides, the presence of more Pd initially will form more $PdZr_2$, requiring more Zr to be added to the fuel in order to maintain the performance of U-10Zr. As the fuel is taken to higher burnup, this becomes a substantial amount of non-fissionable material in the fuel. These are some of the factors involved in determining how much Pd should be added to the fuel, although an ideal ratio of Pd to lanthanides has not been determined at this point.

Both phases present in the Ln-Pd alloy, LnPd and Ln_7Pd_3, are apparent in the SEM images shown in Figure 4. The EDS data for these phases are very consistent, with an average composition of 30Nd-9Ce-7Pr-2La-52Pd at. % (LnPd) for the precipitates, and 35Nd-18Ce-10Pr-5La-32Pd at. % (Ln_7Pd_3) for the bulk matrix material. At this concentration of Pd and lanthanides, the microstructure should be dominated by Ln_7Pd_3 with very little LnPd. That is the case in the microstructure of the

irradiated fuel, shown in Figure 4. The Ln-Pd alloy is lanthanide rich, but not as rich as was intended, due to the loss of lanthanides to lanthanide oxides. The presence of oxygen does not affect the phases present, only the relative amount of each phase and possibly the composition of the phases. Ternary compounds of Pd-Ln-O are known [41] and could form in this system, although there is no spectroscopic evidence for these ternary compounds. The effect of the oxide phase is further discussed below.

EPMA was performed on the Ln-Pd alloy to more accurately determine the composition of each phase. The lanthanide peaks in EDS have significant overlap, thus the deconvolution of peaks will affect the measured composition. Measuring physical standards on the EPMA enables the quantitative measurement of overlapping peaks, thus allowing a more precise peak overlap correction. In addition, WDS spectroscopy has an energy resolution of about 10 eV, compared to approximately 125 eV using the SDD-EDS detector employed by the SEM. Due to the energy resolution of WDS spectroscopy, peak overlap is minimized by using the EPMA. The average EPMA composition obtained for Ln_7Pd_3 is 37.1Nd-17.3Ce-11.4Pr-4.4La-29.9Pd at. %, Table 7. Comparing to the SEM EDS measured compositions listed in Table 6, all of the elements are relatively close, within ~ 2 at. %. The average EPMA composition obtained for LnPd is 31.4Nd-9.1Ce-7.7Pr-2.2La-49.6Pd at. %. The SEM EDS values are again within ~2 at. % of the EPMA values. These results indicate the deconvolution of the lanthanide peaks in SEM-EDS is very good.

Normalizing the EPMA measured average compositions (Table 7) of the lanthanides in Ln_7Pd_3 without Pd yields 52.8Nd-24.6Ce-16.2Pr-6.3La at. %, while the normalized composition in LnPd without Pd is 62.3Nd-18.1Ce-15.3Pr-4.4La at. %. Normalizing in this way does not take mass balance effects in the melt into account, but allows the percentage of each lanthanide present in the phases to be determined for comparison. The lanthanide composition in Ln_7Pd_3 is essentially identical to the lanthanide target composition of 52.3Nd-25.4Ce-16.2Pr-6.1La at. %. This is not the case in LnPd, though, which is high in Nd by 10.0 at. %, and low in Ce (by 7.3 at. %), Pr (by 0.9 at. %) and La (by 1.7 at. %). Taken together, the overall composition of the lanthanides is high in Nd and low in Ce. This discrepancy in the mass balance can be accounted for in the intergranular oxides. The ratio of lanthanides measured with the EPMA in the oxides (removing oxygen and ~2 at. % Pd from the measurements) is 38.6Nd-36.6Ce-16.7Pr-8.1La at. %, so is low in Nd and high in Ce. In the cluster analysis performed on the images collected in the EPMA, 9% of the surface was the intergranular lanthanide oxide phase, so the amount of lanthanides present in the oxide phase on this surface is 3.5Nd-3.3Ce-1.5Pr-0.7La at. %. The LnPd phase makes up 12% of the surface, with a normalized (removing Pd) Ln concentration of 62.3Nd-18.1Ce-15.3Pr-4.4La at. %, making the Ln concentration in LnPd 7.5Nd-2.2Ce-1.8Pr-0.5La at. %. With the oxide being 9% and the LnPd phase being 12%, Nd being high and Ce being low could be attributed to the presence of the oxide phase. This deviation from the target lanthanide composition has also been observed in fuel alloys containing Pd as an additive, with lanthanides added to simulate fission

product lanthanides. For example, in U-10Zr-3.86Pd-4.7Ln wt. % [16], the normalized Ln content in LnPd is 59Nd-17Ce-17Pr-7La at. % and the normalized Ln content in Ln_7Pd_3 is 47Nd-26Ce-17Pr-10La at. %. In a different Pd-containing alloy, U-15Zr-1.6Pd-2.15Ln wt. % [13], the normalized lanthanide composition in the LnPd phase is 72Nd-12Ce-10Pr-6La at. %. In both alloys, the LnPd intermetallic is high in Nd and low in Ce, as observed in the EPMA measurements. These ratios are observed when there is no appreciable lanthanide oxide present in the alloy, but there was oxide present in the melt during fabrication. The low density lanthanide-oxides do not incorporate into the U-Zr alloys, but are left as dross when the pin is cast. Due to this, the lower Ce content in the LnPd phase could be due to Ce being preferentially pulled into the oxide phase, or the lower Ce content in the LnPd phase could be due to the lanthanides in the LnPd crystal structure not being a true solid solution. There may be preference for some lanthanides in the crystal structure over others, leaving the remainder as an oxide dross. Regardless of the reason, the LnPd phase exhibits low Ce, while the Ln_7Pd_3 phase is close to the target lanthanide ratio.

In the lanthanide alloy (Ln alloy), the four lanthanides form a substitutional solid solution with the hexagonal space group *$P6_3/mmc$*. Based on the Hume-Rothery rules, this was expected. The lanthanides are very close in atomic radius, have the same covalency, have essentially the same electronegativity, and all exhibit the *$P6_3/mmc$* crystal structure at room temperature. There is no ternary or quaternary phase diagram information available, but binary phase diagrams exist for all combinations of Nd, Ce, Pr, and La. Only two combinations, Ce-La [42] and Nd-Pr [43], are miscible at all compositions and temperatures. The other four, Nd-Ce [44], Ce-Pr [45], Nd-La [46], and Pr-La [47], all have regions of immiscibility, although they all show complete miscibility at room temperature.

The measured lattice parameters from neutron diffraction for the Ln alloy are a = 3.6774(4) Å and c = 11.8563(5) Å (Table 8 in Section 3.5). Being a solid solution, the lattice parameters were evaluated to determine if this alloy follows Vegard's Law. Using the weighted fraction of room temperature hexagonal lattice constants [48][49] for each of the four elements in 52.3Nd-25.4Ce-16.2Pr-6.1La at. %, the lattice constants of the solid solution should be a = 3.6710 Å and c = 11.8280 Å. There is excellent agreement between the calculated and measured lattice parameters, with the difference being less than 1% for both a and c, indicating the alloy does follow Vegard's Law. In the irradiated annular U-10Zr fuel, the calculated lattice parameters based on the interplanar distance are a = 3.89 Å and c = 12.55 Å (Section 3.1). This is a 6% expansion in each of the parameters, a and c, so is very good agreement considering the differences in these samples. The out-of-pile neutron diffraction was performed on a representative lanthanide composition, but it does not include other fission products. The EDS analysis listed in Table 4 shows Y, Zr, Sm, and a trace amount of U are also present in the irradiated sample. Zr has essentially no solubility in any of the measured elements, and is likely present as sub-nanometer precipitates, below the detection limit of the instrument. The deviation in lattice parameters may be caused by the error associated with measuring lattice parameters using diffraction analysis performed on a TEM. A small amount of error can

be introduced by the instrument setup and calibration, and due to any strain in the sample lamella.

5. Conclusions

This investigation is the characterization of the Ln alloy 52.3Nd-25.4Ce-16.2Pr-6.1La at. %, Pd-Ln alloy, 36.2Nd-17.6Ce-11.2Pr-4.3La-30.7Pd at. %, and Pd-La alloy 69.7La-30.3Pd at. % by neutron diffraction, SEM, and EPMA, as well as the TEM characterization of a lanthanide precipitate in an irradiated annular U-10Zr fuel pin. In addition, Pd-Ln precipitates in a previously characterized irradiated U-10Zr MFF3 fuel pin are shown for comparison to the out-of-pile data. The following conclusions can be drawn from the data presented:

- The composition of the Ln alloy used as a fission product surrogate in out-of-pile studies has been confirmed in three separate U-10Zr irradiations.
- The lanthanide nodules deposited around the periphery of the pores in the irradiated annular U-10Zr pin support the proposed liquid-like transport mechanism for the lanthanides moving through the interconnected pores towards the fuel periphery and cladding.
- The Ln alloy is a solid solution, forming a hexagonal unit cell. Calculating the lattice parameters using a weighted fraction of the lattice parameters of the constituents generates nearly identical parameters as measured by neutron diffraction. The difference is less than 1% for either a or c. This solid solution follows Vegard's Law with no deviation.
- The lattice parameters determined for the lanthanide precipitate in the irradiated annular U-10Zr fuel are slightly larger than the out-of-pile study, but still very close, with only a 6% change in the a and c parameters. This small difference could be due to error associated with determining lattice parameters from the diffraction analysis performed on the TEM.
- The standard-less SEM deconvolution and quantification of the overlapping lanthanide peaks compares very well with the quantification performed with EPMA using physical standards.

Acknowledgments

This work was supported by the U.S. Department of Energy, Office of Nuclear Energy under DOE Idaho Operations Office Contract DE-AC07-05ID14517. This manuscript has also been authored in part by a contractor from UT-Battelle, LLC under Contract No. DE-AC05-00OR22725 with the US Department of Energy (DOE). Accordingly, the U.S. Government retains and the publisher, by accepting the article for publication, acknowledges that the U.S. Government retains a nonexclusive, paid-up, irrevocable, worldwide license to publish or reproduce the published form of this manuscript or allow others to do so, for U.S. Government purposes.

U.S. Department of Energy Disclaimer

References

[1] D.D. Keiser Jr., "Fuel cladding chemical interaction in metallic sodium fast reactor fuels: A historical perspective", *J. Nucl. Mater.*, **2019**, *514*, 393-397.

[2] C. Matthews, C. Unal, J. Galloway, D.D. Keiser Jr., S.L. Hayes, "Fuel-Cladding Chemical Interaction in U-Pu-Zr Metallic Fuels: A Critical Review", *Nucl. Technol.*, **2017**, *198*, 231-259.

[3] Y. Xie, J. Zhang, X. Li, J.P. Isler, M.T. Benson, R.D. Mariani, C. Unal, "Lanthanide Migration and Immobilization in Metallic Fuels", *Prog. in Nucl. Ener.*, **2018**, *109*, 233-238.

[4] S.D. Herrmann, S. Li, *Nucl. Tech.*, **2010**, *171*, 247-265.

[5] G.L. Hofman, L.C. Walters, T.H. Bauer, Metallic fast reactor fuels, *Prog. Nucl. Energy*, **1997**, *31*, 83-110.

[6] H.J. Ryu, B.O. Lee, S.J. Oh, J.H. Kim, C.B. Lee, "Performance of FCCI barrier foils for U–Zr–X metallic fuel", *J. Nucl. Mater.*, **2009**, *392*, 206–212.

[7] J.H. Kim, H.J. Ryu, J.H. Baek, S.J. Oh, B.O. Lee, C.B. Lee, Y.S. Yoon, "Performance of a diffusion barrier under a fuel–clad chemical interaction (FCCI)", *J. Nucl. Mater.*, **2009**, *394*, 144–150.

[8] V. Firouzdor, J. Brechtl, L. Wilson, B. Semerau, K. Sridharan, T.R. Allen, "Development of titanium diffusion barrier coatings for mitigation of fuel–cladding chemical interactions", *Surf. Coat. Technol.*, **2013**, *219*, 59–68.

[9] M.T. Benson, J.A. King, R.D. Mariani, M.C. Marshall, "SEM characterization of two advanced fuel alloys: U-10Zr-4.3Sn and U-10Zr-4.3Sn-4.7Ln," *J. Nucl. Mater.*, **2017**, *494*, 334-341.

[10] Y. Xie, M.T. Benson, J.A. King, R.D. Mariani, J. Zhang, "Characterization of U-Zr fuel with alloying additive Sb for immobilizing fission product lanthanides," *J. Nucl. Mater.*, **2018**, *498*, 332–340.

[11] M.T. Benson, Y. Xie, J.A. King, K.R. Tolman, R.D. Mariani, I. Charit, J. Zhang, M.P. Short, S. Choudhury, R. Khanal, N. Jerred, "Characterization of U-10Zr-2Sn-2Sb and U-10Zr-2Sn-2Sb-4Ln to assess Sn+Sb as a mixed additive system to bind lanthanides", *J. Nucl. Mater.*, **2018**, *510*, 210-218.

[12] R. Khanal, N. Jerred, M.T. Benson, D.A. Andersson, R.D. Mariani, I. Charit, S. Choudhury, "A Novel Approach to Selection of Dopant to Immobilize Neodymium in Uranium-Based Metallic Fuels", *J. Nucl. Mater.*, **2020**, *529*, 151922.

[13] R.D. Mariani, D.L. Porter, T.P. O'Holleran, S.L. Hayes, J.R. Kennedy, "Lanthanides in metallic nuclear fuels: Their behavior and methods for their control," *J. Nucl. Mater.*, **2011**, *419*, 263–271.

[14] J.M. Harp, H.J.M. Chichester, L. Capriotti, "Postirradiation examination results of several metallic fuel alloys and forms from low burnup AFC irradiations," *J. Nucl. Mater.,* **2018,** *509*,

377-391.
[15] M.T. Benson, L. He, J.A. King, R.D. Mariani, “Microstructural characterization of annealed U-12Zr-4Pd and U-12Zr-4Pd-5Ln: Investigating Pd as a metallic fuel additive,” *J. Nucl. Mater.*, **2018**, *502*, 106-112.
[16] M.T. Benson, L. He, J.A. King, R.D. Mariani, A.J. Winston, J.W. Madden, “Microstructural characterization of as-cast U-20Pu-10Zr-3.86Pd and U-20Pu-10Zr-3.86Pd-4.3Ln,” *J. Nucl. Mater.*, **2018**, *508*, 310–318.
[17] M.T. Benson, Y. Xie, L. He, K.R. Tolman, J.A. King, J.M. Harp, R.D. Mariani, B.J. Hernandez, D.J. Murray, B.D. Miller, "Microstructural characterization of annealed U-20Pu-10Zr-3.86Pd and U-20Pu-10Zr-3.86Pd-4.3Ln", *J. Nucl. Mater.*, **2019**, *518*, 287-297.
[18] J. M. Harp, D. L. Porter, B. D. Miller, T. L. Trowbridge, W. J. Carmack, “Scanning electron microscopy examination of a Fast Flux Test Facility irradiated U-10Zr fuel cross section clad with HT-9,” *J. Nucl. Mater.*, **2017**, *494*, 227–239.
[19] J.M. Harp, L. Capriotti, D.L. Porter, J.I. Cole, “U-10Zr and U-5Fs: Fuel/cladding chemical interaction behavior differences,” *J. Nucl. Mater.*, **2020**, *528*, 151840.
[20] L. Capriotti, J.M. Harp, “Characterization of a minor actinides bearing metallic fuel pin irradiated in EBR-II,” *J. Nucl. Mater.*, **2020**, *539*, 152279.
[21] K.E. Wright, J.M. Harp, L. Capriotti, “Electron probe microanalysis of irradiated FUTURIX-FTA U-Pu-Zr alloy with added minor actinides,” *J. Nucl. Mater.*, **2019**, *526*, 151745.
[22] L. Capriotti, S. Brémier, K. Inagaki, P. Pöml, D. Papaioannou, H. Ohta, T. Ogata, V.V. Rondinella, “Characterization of metallic fuel for minor actinides trans- mutation in fast reactor,” *Prog. Nucl. Ener.*, **2017**, *94*, 194e201.
[23] J.M. Harp, L. Capriotti, H.J.M. Chichester, “Postirradiation Examination of FUTURIX-FTA metallic alloy experiments,” *J. Nucl. Mater.*, **2019**, *515*, 420e433.
[24] S. Brémier, K. Inagaki, L. Capriotti, P. Pöml, T. Ogata, H. Ohta, V.V. Rondinella, “Electron probe microanalysis of a METAPHIX UPuZr metallic alloy fuel irradiated to 7.0 at. % burn-up,” *J. Nucl. Mater.*, **2016**, *480*, 109-119.
[25] A.G Croff, “A User’s Manual for the ORIGEN2 Computer Code,” ORNL/TM-7175, Oak Ridge National Laboratory, July 1980.
[26] A.L. Pitner, R.B. Baker, “Metal fuel test program in the FFTF,” *J. Nucl. Mater.*, **1993**, *204*, 124-130.
[27] W.J. Carmack, H.M. Chichester, D.L. Porter, D.W. Wootan, “Metallography and fuel cladding chemical interaction in fast flux test facility irradiated metallic U-10Zr MFF-3 and MFF-5 fuel pins,” *J. Nucl. Mater.*, **2016**, *473*, 167-177.
[28] C.T. Chantler, “Theoretical Form Factor, Attenuation, and Scattering Tabulation for Z=1–92 from E=1–10 eV to E=0.4–1.0 MeV,” *J. Phys. Chem. Ref. Data*, **1995**, *24*, 71–643.
[29] J.T. Armstrong, “Quantitative analysis of silicate and oxide materials: comparison of monte carlo, ZAF, and ψ (ρz) procedures,” *Microbeam Anal.*, **1988**, 239–246.
[30] V.D. Scott, G. Love, "Quantitative Electron-Probe Microanalysis", E. Horwood, New York, 1983.
[31] H.M. Reitveld, “A profile refinement method for nuclear and magnetic structures,” *J. Appl. Crystallogr.*, **1969**, *2*, 65-71.
[32] B.H. Toby, "EXPGUI, a graphical user interface for GSAS" *J. Appl. Crystallogr*., **2001**, *34*, 210-213.
[33] T. Yao, L. Capriotti, X. Liu, Y. Wang, J.M. Harp, J. Gan, M.T. Benson, L. He, "α-U and ω-UZr_2 in Neutron Irradiated U-10Zr Annular Metallic Fuel", *J. Nucl. Mater.*, **2020**, *542*, 152536.
[34] X. Liu, L. Capriotti, T. Yao, J.M. Harp, M.T. Benson, Y. Wang, L. He, "Fuel-cladding chemical interaction of a prototype annular U-10Zr fuel with HT-9 cladding", J. Nucl. Mater., submitted.
[35] G.C. Che, J. Liang, Y. Yi, *Jinshu Xuebao*, **1986**, *22*, B206.
[36] H. Okamoto, “Nd-Pd (Neodymium-Palladium),” *J. Phase Equilibria*, **1992**, *13*, 220–222.
[37] X. Li, J. Zhang, C. Unal, R.D. Mariani, “Behaviors of Ce, Pr, and Nd in liquid cesium by ab initio molecular dynamics simulations”, *J. Appl. Phys.*, **2018**, *124*, 135102.

[38] J.P. Isler, “Interactions of lanthanides and liquid alkali metals for “liquid-like” lanthanide transport in U-Zr Fuel,” Master thesis (The Ohio State University, 2017).
[39] J. Isler, J. Zhang, R. Mariani, C. Unal, “Experimental solubility measurements of lanthanides in liquid alkalis”, J. Nucl. Mater., 2017, 495, 438-441.
[40] H. Okamoto, Cs-Pr (Cesium-Praseodymium), Binary Alloy Phase Diagrams, II Ed., Ed. T.B. Massalski, **1990**, 2, 1384-1385.
[41] K.T. Jacob, T.H. Okabe, T. Uda, Y. Waseda, “System Nd-Pd-O: Phase Diagram and Thermodynamic Properties of Oxides Using a Solid-State Cell with Advanced Features”, *J. Phase Equilib.*, **1999**, *20*, 553-564.
[42] K.A. Gschneidner Jr., F.W. Calderwood, Ce-La (Cerium-Lanthanum), Binary Alloy Phase Diagrams, II Ed., Ed. T.B. Massalski, **1990**, 2, 1075-1077.
[43] K.A. Gschneidner Jr., F.W. Calderwood, Nd-Pr (Neodymium-Praseodymium), Binary Alloy Phase Diagrams, II Ed., Ed. T.B. Massalski, **1990**, 3, 2794-2797.
[44] K.A. Gschneidner Jr., F.W. Calderwood, Ce-Nd (Cerium-Neodymium), Binary Alloy Phase Diagrams, II Ed., Ed. T.B. Massalski, **1990**, 2, 1085-1087.
[45] K.A. Gschneidner Jr., F.W. Calderwood, Ce-Pr (Cerium-Praseodymium), Binary Alloy Phase Diagrams, II Ed., Ed. T.B. Massalski, **1990**, 2, 1095-1098.
[46] K.A. Gschneidner Jr., F.W. Calderwood, La-Nd (Lanthanum-Neodymium), Binary Alloy Phase Diagrams, II Ed., Ed. T.B. Massalski, **1990**, 3, 2405-2406.
[47] H. Okamoto, La-Pr (Lanthanum-Praseodymium), Binary Alloy Phase Diagrams, II Ed., Ed. T.B. Massalski, **1990**, 3, 2411-2413.
[48] F.H. Spedding, A.H. Daane, K.W. Herrmann, “The Crystal Structures and Lattice Parameters of High-Purity Scandium, Yttrium and the Rare Earth Metals,” *Acta Crystallogr.*, **1956**, *9*, 559-563.
[49] K.A. Gschneidner Jr., R.O. Elliott, R.R. McDonald, “Effects of alloying additions on the γ <-> α transformation of cerium. Part I. Pure cerium,” *Phys. Chem. Solids*, **1962**, *23*, 555-566.